

Numerical simulation of a two-dimensional internal wave attractor

NICOLAS GRISOUARD, CHANTAL STAQUET
AND IVANE PAIRAUD

Laboratoire des Écoulements Géophysiques et Industriels, BP 53, 38041 Grenoble Cedex 9, France

(Received 9 January 2008 and in revised form 23 June 2008)

Internal (gravity) wave attractors may form in closed containers with boundaries non-parallel and non-normal to the gravity vector. Such attractors have been studied from a theoretical point of view, in laboratory experiments and using linear numerical computations. In the present paper two-dimensional numerical simulations of an internal wave attractor are reported, based upon the nonlinear and non-hydrostatic MIT-gcm numerical code. We first reproduce the laboratory experiment of a wave attractor performed by Hazewinkel *et al.* (*J. Fluid Mech.* Vol. 598, 2008 p. 373) and obtain very good agreement with the experimental data. We next propose simple ideas to model the thickness of the attractor. The model predicts that the thickness should scale as the $1/3$ power of the non-dimensional parameter measuring the ratio of viscous to buoyancy effects. When the attractor is strongly focusing, the thickness should also scale as the $1/3$ power of the spatial coordinate along the attractor. Analysis of the numerical data for two different attractors yields values of the exponent close to $1/3$, within 30 %. Finally, we study nonlinear effects induced by the attractor.

1. Introduction

Stably stratified fluids are encountered in geophysics and astrophysics, examples being the oceanic thermocline, the stratosphere and the radiative zone of the Sun. From a mechanical point of view, any non-horizontal motion in these fluids yields a restoring force, namely the buoyancy force, which generates internal gravity waves. (The Coriolis force due to the rotation of the system – such as a star – may also act as a restoring force.) These waves are dispersive with a very specific dispersion relation: their frequency depends upon the angle θ of the wave vector with respect to the gravity vector. In an unlimited medium with a constant stable gradient of density, the dispersion relation is indeed $\omega = N \cos \theta$, where ω is the frequency of the waves and N is the buoyancy frequency (whose square is proportional to the stable gradient of density). As a consequence, phase and energy propagate perpendicularly to each other (e.g. Lighthill 1978). As first noted by Phillips (1967), the peculiar form of the dispersion relation leads to a peculiar wave reflection at a wall inclined with respect to the gravity vector: because ω is preserved upon reflection, the angle θ is preserved as well, which leads to focusing or defocusing of the waves after reflection.

In closed domains, multiple reflections with more focusing than defocusing at the boundaries can lead to the formation of a wave attractor, namely a part of the domain where almost all the wave-induced energy is concentrated, as shown by Maas & Lam (1995). From a mathematical point of view, the existence of the attractor stems from the fact that the inviscid linear equations of motions are spatially hyperbolic

(when a harmonic time-dependence is imposed) while boundary conditions must be satisfied on the walls of the closed domain. The problem is therefore ill-posed in the absence of viscosity. Singular solutions, distinct from the usual (regular) normal modes, may arise which eventually converge toward an attractor as time elapses. The introduction of viscosity regularizes the equation, which becomes elliptic (Rieutord, Georgeot & Valdetaro 2001). But the attractor appears again in the viscous solution when viscosity effects are low enough with respect to restoring effects. This was shown by Rieutord & Valdetaro (1997) in the astrophysical context for a rotating shell. As analysed by Rieutord & Noui (1999) and Ogilvie (2005), these results are valid whether the restoring force is the buoyancy force or the Coriolis force in a rotating system. These works ensure that the structure and dynamics of a wave attractor can be studied numerically by solving directly the viscous equations of motions, provided the viscosity is low enough. From a practical point of view, this implies that the grid size should be much smaller than the thickness of the attractor, namely, the resolution should be high enough to satisfy this requirement.

Most studies on internal wave attractors are theoretical, focusing on the derivation of analytical models for the attractors, with and without viscosity. Experimental work was performed recently, starting with laboratory evidence of an internal wave attractor in a trapezoidal stably stratified water tank (Maas *et al.* 1997). The data of the latter experiment were reanalysed by Lam & Maas (2008) and further experimental studies were performed by Hazewinkel *et al.* (2008) (hereafter referred to as HBDM 08).

Nearly all numerical studies of wave attractors solve the linear equations of motions (Rieutord *et al.* 2001; Rieutord, Valdetaro & Georgeot 2002; Ogilvie 2005). In the recent paper by Drijfhout & Maas (2007), a nonlinear hydrostatic numerical ocean model is used to investigate the dynamics of trapped waves in a closed channel in the vicinity of a continental slope, but the forcing amplitude is tuned so that the flow dynamics is linear at all times. To our knowledge, no attempt has been made yet to investigate the fine structure of the attractor and its nonlinear behaviour by means of nonlinear direct numerical simulations. This is the aim of the present paper. The MIT general circulation model is used for this purpose at a high resolution so that a low viscosity can be used, as discussed above. The results are carefully validated against the laboratory experiment of HBDM08 to test the ability of the numerical code to reproduce the singular solution associated with the attractor. In §2, we present the experimental and numerical setups, while the comparison between the numerical and experimental results is reported in §3. In §4 we propose a simple model for the thickness of the wave attractor, which we test against our numerical data and relate to the theoretical work by Thomas & Stevenson (1972). Insight into the nonlinear behaviour of the wave attractor is presented in §5 before we draw conclusions in the final section.

2. Laboratory and numerical setups

2.1. Laboratory experiment of HBDM08

The height and width of the tank in the experiment are respectively equal to 200 mm and 101 mm; the length of the tank varies from 353 mm at the upper boundary to 453 mm at the bottom boundary, due to the presence of a sloping wall that makes an angle $\alpha = 27^\circ$ with the vertical (see figure 2 below).

The stratification is imposed by salt water whose density decreases linearly upwards, with $N_{lab} \simeq 3.0 \text{ rad s}^{-1}$. However, because the density flux through the free surface and bottom boundary is equal to zero, the stratification cannot be maintained there

and very thin diffusive mixed layers slowly develop from these boundaries. The experimental viscosity has a value of $1 \text{ mm}^2 \text{ s}^{-1}$, the Prandtl number of salt water being equal to 700. The forcing mechanism of the wave field is as follows. Starting from rest, the tank is subjected to an oscillation at frequency $\omega_e = 1.23 \text{ rad s}^{-1}$ (associated with a period $T = 5.11 \text{ s}$), leading to the generation of a wave field at the same frequency. The frequency and tank geometry have been chosen so that a wave field develops and gets focused toward an attractor.

This is the experiment we reproduce numerically, apart from some differences which we explain below.

2.2. Numerical setup

The MIT general circulation model is used to solve the nonlinear, non-hydrostatic, incompressible Boussinesq equations that govern the fluid dynamics (see Marshall *et al.* 1997). No subgrid scale modelling is used in the present work, implying that the simulations are direct (i.e. the diffusion operator is the ordinary Laplacian operator).

The symmetry of the forcing as well as the narrow width of the tank in the laboratory experiment implies that the dynamical processes should be mainly two-dimensional in a vertical plane; hence, in the numerical experiment, a two-dimensional domain is used for simplicity. We also flip this numerical domain in the z -direction so that the wall becomes of positive slope and can be easily handled by the code (we also reverse the density field so that the stratification remains stable). The Boussinesq equations are indeed invariant under this transformation.

We were able to reproduce the same attractor as in the laboratory experiment by setting N to the value of 2.76 rad s^{-1} (instead of 3 rad s^{-1}). We think that the origin of this difference lies in the thickness of the mixed layers which develop at the free surface and at the bottom of the tank, which are slightly different in the experiment and in the simulation. Indeed, the attractor reflects onto these mixed layers.

To speed up the convergence towards the attractor, we chose the following forcing. A barotropic current oscillating at frequency ω_e and of amplitude $7.38 \times 10^{-2} \text{ mm s}^{-1}$ is imposed at the vertical boundary to force the flow. This amplitude has been chosen to ensure that a linear regime sets in, as in the laboratory experiment. (To analyse nonlinear effects in §5, we carried out the same computation with a ten-times larger amplitude.) In the laboratory experiment, the forcing regime is imposed over $50T$ and then turned off. In the simulation, the forcing regime is turned off after $61T$, to lengthen this regime and improve the statistics. The subsequent decay stage is monitored over $51T$.

Viscosity is set to $\nu = 1 \text{ mm}^2 \text{ s}^{-1}$, as in the laboratory experiment, while the Prandtl number has a value of 100. (A higher value of this parameter would lead to ill-resolved smallest diffusive scales.)

Free-surface and free-slip conditions on the three other boundaries are set to prevent under-resolved viscous boundary layers from appearing. However, the forcing chosen requires an open-boundary condition on the vertical wall, which cancels the free-slip condition at this boundary (the vertical velocity being set to zero there). As a consequence, a very thin shear layer appears on the vertical wall during the forced stage which quickly vanishes (in approximately $3T$) after forcing is turned off.

We use a Cartesian grid with horizontal and vertical grid sizes equal to $dx = dz = 0.5 \text{ mm}$, the cells being shaved on the sloping wall to allow for the reflection of the wave field. As we show in §4, the thickness of the attractor is around 45 mm wide, which is therefore described by 90 points. One period is discretized into 250 time steps (implying that $dt = 0.02044 \text{ s}$).

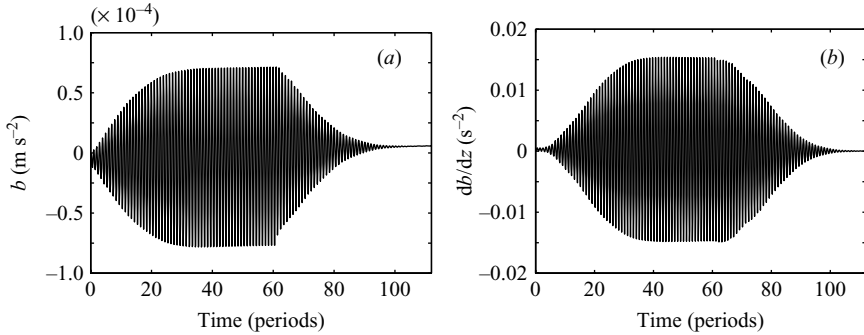


FIGURE 1. (a) Evolution of the buoyancy field b as a function of time, at a point located in the central part of the attractor along section S_1 displayed in figure 2. (b) Same as (a) but for $\partial_z b$.

In the following sections measurements of the buoyancy $b = -g \rho' / \rho_0$ are displayed, where ρ_0 is a constant reference density and ρ' is the density perturbation, computed as the difference between the instantaneous density field and the initial density profile.

3. Comparison with the laboratory experiment of HBDM08

3.1. Overall behaviour of the fluid motions

The buoyancy field b is displayed versus time in figure 1(a) at a fixed location within the attractor. Three regimes can be distinguished. From initial time until $t \simeq 30T$, the amplitude of the oscillations grows as the wave field organizes itself into an attractor. A stationary regime is then reached, once the attractor has formed, implying that some equilibrium has occurred; note that the mean (temporally averaged) buoyancy is slightly negative because of forcing. The equilibrium regime ceases at $61T$, when forcing is turned off, and the flow relaxes to rest through decaying oscillations. The buoyancy field being computed as the difference between the instantaneous density profile and the initial profile (up to a multiplicative constant), the non-zero final value of b attests to the fact that mixing has been induced.

As in HBDM08, in which the synthetic schlieren method is used, we computed the vertical gradient of the buoyancy field, $\partial_z b$, as a function of time (figure 1b). The remarkable point is that the maximum amplitude of this field remains unchanged during a few periods after forcing has been turned off. Since the amplitude of b decays, this implies that the vertical scale associated with the buoyancy field decreases after the forcing is turned off, thus compensating for the decay in amplitude of b . This point is further discussed below.

To visualize the attractor, we follow HBDM08 and filter the field $\partial_x b$ at frequency ω_e during the equilibrium regime. The filtered field, denoted $B_{\omega_e}(x, z)$, is defined by

$$B_{\omega_e}(x, z) = \frac{2}{T} \int_{t_i}^{t_f} [\partial_x b(x, z, t)] e^{i\omega_e(t-t_i)} dt, \quad (3.1)$$

with $t_i = 40T$ and $t_f = 61T$.

The modulus $|B_{\omega_e}|$ of the filtered field is displayed in figure 2(a), thereby showing the spatial distribution of the amplitude. The attractor predicted by ray theory, namely the trajectory of the wave-induced energy at large times, is also displayed with a

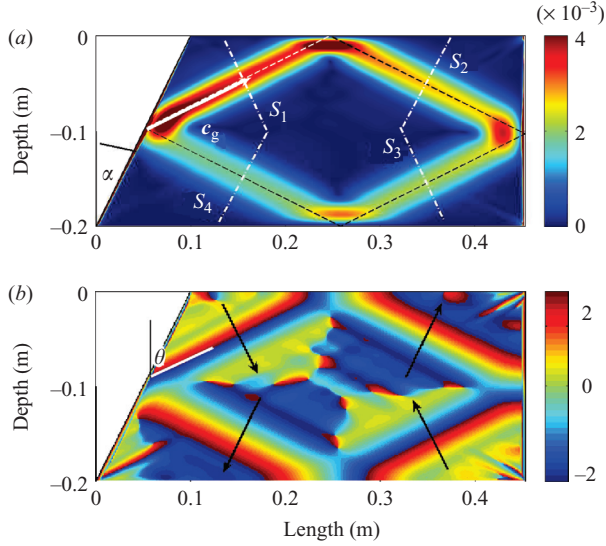


FIGURE 2. Harmonic analysis of $\partial_x b$ from $t=40T$ to $t=61T$. (a) Amplitude field. The white arrow points towards the direction of the group velocity \mathbf{c}_g and the four sections S_1 – S_4 used in the analysis are displayed (the slope angle α is also shown). The location of the attractor as predicted by ray theory is indicated with a dashed line. (b) Phase field. The black arrows point toward the direction of phase propagation, or \mathbf{k} , for each branch; the propagation angle θ is shown.

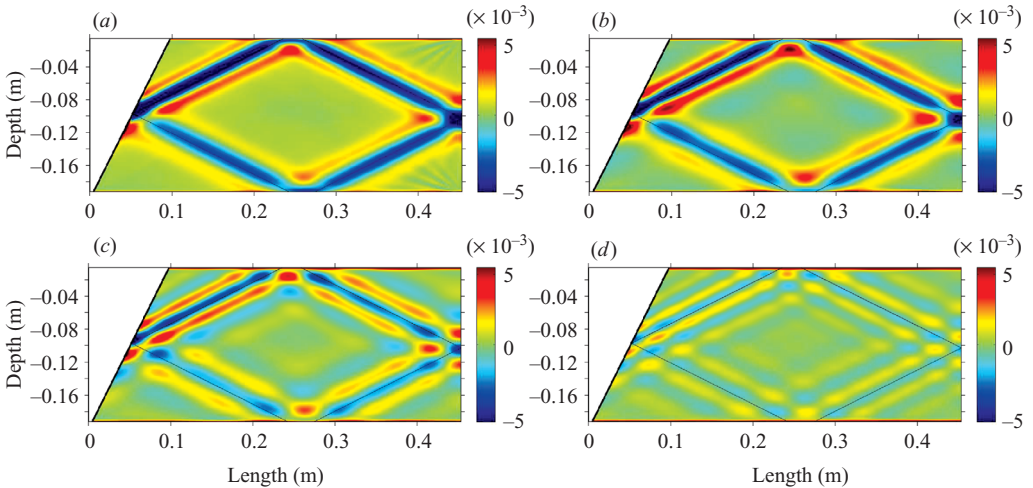


FIGURE 3. Constant contours of $\partial_z b$ at (a) $t=63T$, (b) $t=71T$, (c) $t=79T$, (d) $t=87T$. The location of the attractor as predicted by ray theory is indicated with a thin black line.

dashed line. Several striking features may be noted in this figure. The amplitude is focused within a well-defined structure – the attractor – made of four branches. The amplitude is maximum at the beginning of the first branch on the inclined wall, where the focusing point is located. The amplitude constantly decays along the attractor when travelling from the focusing point, due to viscous effects. This decrease of the

amplitude provides the direction of the group velocity \mathbf{c}_g which is clockwise, consistent with the direction in which focusing occurs. Precisely the same structure was obtained by HBDM08 in their laboratory experiment. The only difference lies in the values of the amplitude, which cannot be compared because the forcings are different.

To complement figure 2(a), the phase of the buoyancy field at $t = t_f$, given by $\arg(B_{\omega_c} e^{i\varphi})$ with $\varphi = 2\pi(t_f - t_i)/T$, is displayed in figure 2(b). The direction of propagation of the phase can be read directly from this figure (as indicated by the arrows). Assuming the wave field is spatially monochromatic within the attractor, a wave vector \mathbf{k} can be defined, which is aligned with the spatial gradient of the phase. The wavelength associated with \mathbf{k} will be referred to as the apparent wavelength hereafter. Since the vertical component of \mathbf{k} and of the group velocity are of opposite sign for internal gravity waves, the direction of the group velocity can also be inferred from figure 2(b).

The modification of the attractor once forcing has been turned off, from $t = 61T$, is illustrated in figure 3 through contours of $\partial_z b$ plotted at successive times. The apparent wavelength of the attractor decreases with time, suggesting, following HBDM08, that the short wavelengths ‘survive’ longer than the large ones. This striking behaviour is further discussed in the next section and will serve as a precise comparison between our numerical model and the experimental results.

3.2. Spatial structure of the wave attractor

The striking evolution of the apparent wavelength during the decay stage suggests performing a spatial spectral analysis of the wave field. For this purpose, we introduce a natural coordinate system (s, η) , with s the along-branch abscissa starting from the focusing point and oriented in the same direction as \mathbf{c}_g , and η the cross-branch ordinate whose origin is on a branch and oriented to get a direct coordinate system for each branch. We choose four locations, each in the middle of a different branch, and we perform the analyses along the cross-attractor sections which start from these points and which we call S_1 – S_4 . Along S_1 , for instance, we write $\partial_\eta b$ as

$$\partial_\eta b(\eta, t)|_{S_1} = \int_{-\infty}^{+\infty} A(k, t) e^{i(k\eta - \omega t)} dk \quad (3.2)$$

using $k = |\mathbf{k}|$, this analysis also being performed along S_2 – S_4 .

Figure 4 shows the spectra $|A|^2$ of S_1 – S_4 at $t = 50T$ during the equilibrium regime for the simulation and the experiment of HBDM08. Both approaches show that the spectrum is continuous, implying that not just a single scale is involved, and that it displays a maximum, implying that a dominant scale exists. As one progresses along the attractor from S_1 to S_4 , the peak shifts towards small values of k (i.e. large values of wavelength) and the maximum amplitude decreases, because of diffusive effects. This is consistent with the apparent broadening and decaying amplitude of the attractor after the focusing point observed in figure 2.

Despite the qualitative agreement between the simulation and the laboratory experiment, a difference should be noted: the decrease in amplitude along the attractor is stronger in the experiment. This difference might be explained by damping effects being larger in the experiment than in the simulation. It should indeed be emphasized that the experiment is three-dimensional so that boundary layers also exist in the third direction, which provide an additional sink of energy (McEwan 1971). Such boundary layers are prohibited by the two-dimensional geometry of the simulation.

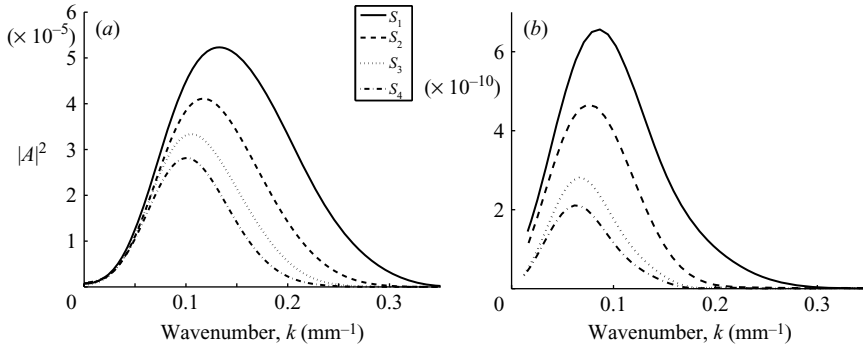


FIGURE 4. Spectral analysis along sections S_1 – S_4 at time $t = 50T$. (a) Results from the numerical simulation. (b) Tank measurements by HBDM08.

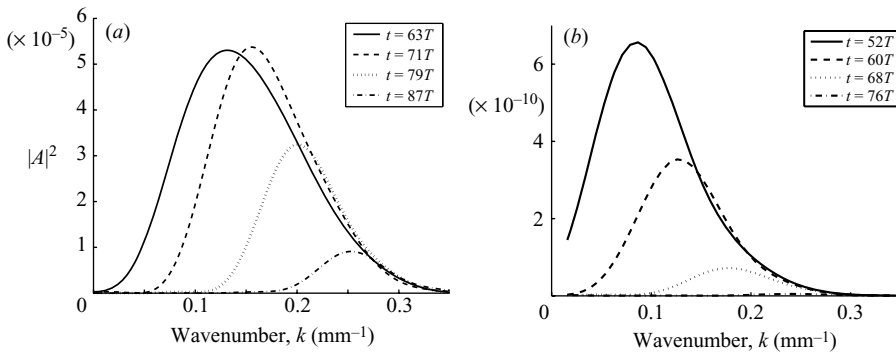


FIGURE 5. Spectral analysis along section S_1 at times $\tau = 2T$, $\tau = 10T$, $\tau = 18T$ and $\tau = 26T$ after forcing has been turned off. (a) Simulation. (b) Experiment of HBDM08.

Spectra of S_1 for the simulation and the experiment are displayed in figure 5 during the decay stage, at different times. It is quite noteworthy that the decay in the total amplitude now goes with a shift of the peak towards high values of k , as implied by figure 1(b), and not toward small values of k , as a simple argument based upon viscous effects would imply. The difference in the evolution of the amplitude between experiment and simulation can still be noted. The amplitude decays less rapidly in the simulation and its maximum value is nearly the same at $63T$ and $72T$. This is consistent with the behaviour observed in figure 1(b) for $\partial_z b$: the reduction in amplitude of the buoyancy is made up for by the decrease of the attractor thickness, so that the amplitude of $\partial_z b$ remains nearly unchanged during several periods after forcing has been turned off. This effect is not visible in the experiment, possibly because of the presence of boundary layers in the third direction, as argued above, which promote energy dissipation.

We again follow HBDM08 to explain the behaviour of these spectra. The forcing excites the largest vertical scale of the tank, which has wavenumber $k_0 = \pi/H$. This new-born wave packet propagates and gets focused at the sloping wall, propagates and gets focused again. This focusing results in a transfer of energy towards high wavenumbers (small scales) and the wavenumber of the wave packet can be considered as a measure of its ‘age’. Viscous damping then acts, and the smaller the scale is, the more efficient this damping is. At the beginning of its life, amplification thus dominates and the amplitude of the wave packet increases; but viscous damping

increases as well, which eventually balances amplification. Seen from a continuous point of view, the balance between focusing and viscous damping in the equilibrium regime results in the spectra displayed in figure 4. When forcing is turned off, creation of low-wavenumber wave packets stops, but not the propagation and reflections of existing wave packets. Their scales get smaller and smaller because of focusing and those wave packets eventually get dissipated. This is what we observed in figures 3 and 5.

4. A simple model for the thickness of the wave attractor

4.1. Model

In the analysis developed in HBDM08 and summarized in the previous section, the spatial structure of the attractor is accounted for by the evolution of a wave packet travelling along the attractor. The apparent wavelength of this wave packet defines a scale, which may be used to characterize the thickness of the attractor. Let us derive a simple model for this scale, referred to as λ in the following.

As in Rieutord *et al.* (2001) and HBDM08, we argue that the thickness of the attractor is set by the competition between focusing, which reduces the scale by a factor $\gamma = \sin(\theta + \alpha)/\sin(\theta - \alpha)$ and diffusion, which makes that scale grow.

Along the attractor, as long as the focusing point is not crossed, the only effect acting on the wave packet is diffusion. Hence, from the diffusion scaling law, $\lambda(d\lambda/dt) = C\nu$, where C is constant and ν is the viscosity. Introducing the coordinate s along the attractor yields $\lambda(d\lambda/ds)(ds/dt) = C\nu$. With $ds/dt = |\mathbf{c}_g| = N(\sin\theta)\lambda/2\pi$, one gets

$$\lambda^2 \frac{d\lambda}{ds} = \frac{2\pi C\nu}{N\sin\theta}. \quad (4.1)$$

We integrate along the attractor over its length L_a in the direction of energy propagation from $s=0^+$ (just after the focusing point) to $s=L_a^-$ (just before it). If this is the n th travel of the wave packet, we get

$$\lambda_n^3(L_a^-) - \lambda_n^3(0^+) = 6\pi C \frac{\nu L_a}{N\sin\theta}. \quad (4.2)$$

When the wave packet crosses the focusing point, its thickness is focused again so that $\lambda_{n+1}(0^+) = \lambda_n(L_a^-)/\gamma$. In the equilibrium regime, $\lambda_{n+1}(0^+) = \lambda_n(0^+)$. It follows that

$$\lambda(0^+) = C'(\gamma^3 - 1)^{-1/3} \left(\frac{\nu L_a}{N\sin\theta} \right)^{1/3}, \quad (4.3)$$

dropping the index n and with $C' = (6\pi C)^{1/3}$. At any location along the attractor, the thickness is therefore defined as

$$\lambda(s) = C' \left(\frac{\nu L_a}{N\sin\theta} \right)^{1/3} \left(\frac{s}{L_a} + \frac{1}{\gamma^3 - 1} \right)^{1/3}. \quad (4.4)$$

Rieutord *et al.* (2001) guessed from their numerical simulations that the thickness of the attractor should scale as $E^{1/3}$, where E is the Ekman number, assumed $\ll 1$; in practice, this parameter should be smaller than 10^{-6} for this scaling to hold. The analogue of the Ekman number in our study is $\nu/(ND^2)$, where D is a typical scale of the attractor. Using $D = L_a$, the values of $\nu/(NL_a^2)$ are smaller than 10^{-6} in our simulation (since $L_a = 954$ mm). And expression (4.4) indeed involves a dependency

on the power $1/3$ of this parameter, when written in a dimensionless manner:

$$\frac{\lambda(s)}{L_a} = C'(\sin\theta)^{-1/3} \left(\frac{\nu}{NL_a^2} \right)^{1/3} \left(\frac{s}{L_a} + \frac{1}{\gamma^3 - 1} \right)^{1/3}. \quad (4.5)$$

Also, in Ogilvie (2005), an asymptotic ($\nu \rightarrow 0$) solution is derived to describe the attractor resulting from a periodic forcing. The derivation fundamentally relies on the assumption that the thickness of the attractor scales like $\nu^{1/3}$, in agreement with our model.

4.2. Analogy with an internal wave beam emitted by an oscillating object

When the focusing parameter γ is much larger than 1, expression (4.4) becomes

$$\lambda_{\gamma \gg 1}(s) = C' \left(\frac{\nu s}{N \sin\theta} \right)^{1/3}. \quad (4.6)$$

This expression is identical to that obtained by Thomas & Stevenson (1972) when modelling the structure of a wave beam emitted by an oscillating two-dimensional object (see also Gostiaux 2006). The emission region is the location where the wave beam is tangent to the object, the direction of the beam being set by the dispersion relation. Since the size of the object does not come into play in this theory, the far-field limit is assumed. In other words, the object is seen as a source point. A length scale still comes into play, which is the thickness of the boundary layer on the object. Expression (4.6) may indeed be written as $C'(\delta^2 s / \tan\theta)^{1/3}$, where $\delta = \sqrt{\nu/\omega}$ is the thickness of the boundary layer.

The analogy of relation (4.6) with the expression of Thomas & Stevenson (1972) may be interpreted as follows. Consider a frame of reference attached to the vertical forcing boundary. In this frame, the inclined wall oscillates and may be considered as the actual source of energy for the wave field. Hence, in this frame, the wave attractor becomes a wave beam emitted by an oscillating object. The emission region is on the inclined wall, at the location where the reflected beam coincides with the incident one. And the thickness δ is that of the boundary layer on the inclined wall. The attractor may then be interpreted as a wave beam emitted by an infinitely small oscillating source located at the focusing point.

The fact that the analogy is obtained for $\gamma \gg 1$ suggests interpreting $1/\gamma$ as the (properly scaled) size of the source. When γ is large, the factor $(\gamma^3 - 1)^{-1/3}$ becomes quickly negligible with respect to s/L_a as one moves away from the source, implying that the source is infinitely far.

4.3. Numerical validation

The validation of relation (4.5) requires the computation of the thickness λ of the attractor. As noted above, the apparent wavelength of the wave packet travelling along the attractor serves as a measure of the attractor thickness. To compute such an apparent wavelength, we plot in figure 6(a) the density perturbation profile across the attractor at a given position and time during the equilibrium regime. As indicated in the figure, an apparent wavelength can be defined, as twice the distance between two extrema of the profile.

The apparent wavelength has therefore been computed from the plot of the density perturbation profile at different locations on the second, third and fourth branches after the focusing point (the first branch being too close to the sloping wall to get proper measurements). λ is plotted against $s/L_a + 1/(\gamma^3 - 1)$ in log-log scale in figure 6(b) to find a possible power relation. Linear regression shows that $\lambda \propto (s/L_a + 1/(\gamma^3 - 1))^{0.229 \pm 0.011}$.

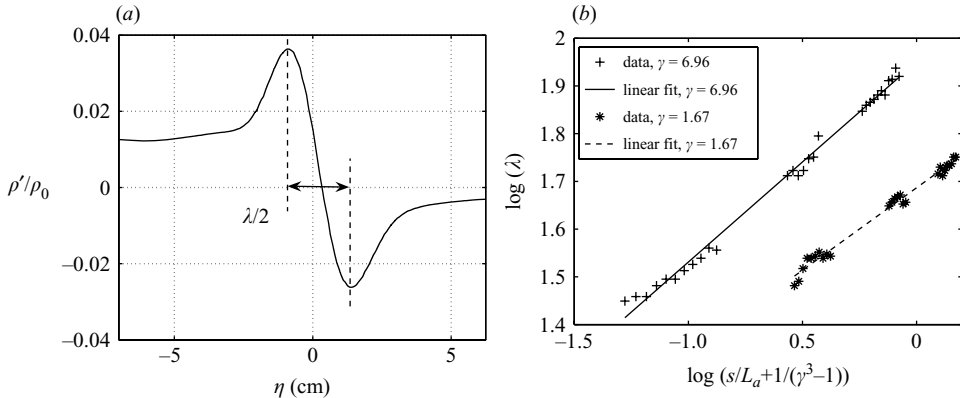


FIGURE 6. (a) Definition of the half-wavelength of the density perturbation field at a given time. (b) Plot of λ as a function of $s/L_a + 1/(\gamma^3 - 1)$ in log-log scale for the configuration with $\gamma = 1.67$ (stars) and the associated linear fit (dashed line), as well as for the configuration with $\gamma = 6.96$ (crosses) and the associated linear fit (solid line).

In this simulation, $\gamma = 1.67$ so that $1/(\gamma^3 - 1)$ is equal to 0.27 and is never small with respect to s/L_a . We therefore ran another simulation with a higher value of γ . This simulation corresponds to the same tank as in the experiment of HBDM08 except that the bottom length is 290 mm instead of 453 mm and the top length is 140 mm instead of 353 mm. It is filled with 300 mm of water, with stratification $N = 2 \text{ rad s}^{-1}$, and the forcing frequency is $\omega_e = 1.65 \text{ rad s}^{-1}$. In this configuration, the beams have a steeper slope with an associated $\gamma = 6.96$. Under this condition, one can approximate expression (4.4) by (4.6) as soon as $s \gg L_a/300 \approx 2.5 \text{ mm}$ (with $L_a = 726 \text{ mm}$ in this case). Results for this simulation are also displayed in figure 6(b). We find $\lambda \propto (s/L_a + 1/(\gamma^3 - 1))^{0.417 \pm 0.015}$.

These two cases show that neither power exponent is equal to $1/3$ but both exponents are close to it, within 30%. The observed discrepancy very likely comes from the main assumption of our (very simple) model, which is that a single scale characterizes the attractor. The spectra displayed in figures 4 and 5 show indeed that only a dominant scale exists among a continuum of scales.

5. Nonlinear effects

5.1. Existence of nonlinear effects

The forcing amplitude in the previous runs was low enough to ensure that a linear regime was reached. To investigate the manifestation of nonlinear effects, we ran a simulation analogous to that described in §3, except that the forcing amplitude is ten times larger. This run is displayed in figure 7, through constant contours of $\partial_z b$ two periods after forcing has been turned off.

Since forcing occurs at frequency ω_e , all motions oscillate at that frequency in a linear regime. Nonlinear effects yield new motions at a harmonic frequency, which are visible in figure 7: steep wave beams at frequency $2\omega_e$, distinct from the attractor, propagate in the domain. Motions at frequency $2\omega_e$ and $3\omega_e$ (using the same filtering method as in §3.1) are displayed in figure 8. Since $2\omega_e/N = 0.89 < 1$, the $2\omega_e$ -field can propagate but, in the present case, does not reach an attractor. As shown in figure 8(a), this field is generated at the locations where the attractor reflects on the vertical and horizontal boundaries. At these locations the superpositions of the branches

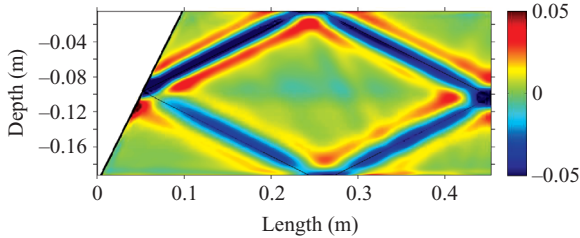


FIGURE 7. Same as figure 3(a), but for a ten times larger forcing amplitude.

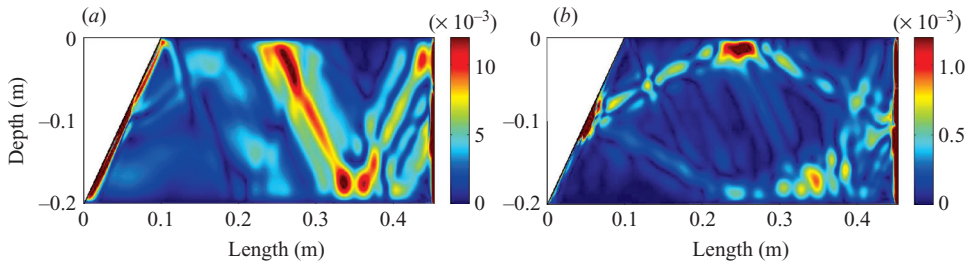


FIGURE 8. Harmonic analysis of $\partial_z b$ from $t = 40T$ to $t = 61T$, filtered at frequencies $2\omega_e$ and $3\omega_e$. (a) $2\omega_e$ -component; (b) $3\omega_e$ -component. Note that the colour scales of the two figures are different.

make the nonlinear terms of the governing equations non-zero, as shown by Tabaei, Akylas & Lamb (2005) in the more general context of wave beams. The focusing point has a particular status in the present case as the $2\omega_e$ beam has a propagation angle equal to the slope of the wall, which is why no emitted beam is clearly observed.

On the other hand, $3\omega_e/N = 1.33 > 1$ so that the $3\omega_e$ -field cannot propagate. Figure 8(b) shows that this motion is trapped within the attractor. Its amplitude is the strongest at the crossings between the ω_e -branches of the attractor and the $2\omega_e$ -beam emitted at the reflection location on the upper boundary, attesting to its nonlinear generation from these two frequency motions.

5.2. Mixing

As shown above, the thickness of the attractor during the equilibrium regime is small, in the sense that it is set by an equilibrium between focusing and viscous effects. Strong gradients of the velocity and fluctuating density fields therefore occur all along the attractor, which result in local mixing of mass. As in any stably stratified fluid, local mixing yields horizontal density, and therefore pressure, gradients so that the mixed fluid travels along iso-density surfaces away from the mixed region (for instance Browand, Guyomar & Yoon 1987; McPhee-Shaw & Kunze 2002). Rieutord & Noui (1999) pointed out the important role wave attractors should play in the transport properties of the flow. More recently Tilgner (2007), using asymptotic expansion of the flow variables in a rotating fluid, was able to show that nonlinear interactions within the attractor could produce a mean flow.

In the present case, we found that the relative change in N due to mixing between initial and final times of the simulation is not larger than 0.3%. This value depends

upon the duration of the forcing stage but is still very weak. Mixing is in fact usually small in a uniformly stratified fluid because the scale of the density profile is the height of the tank container, which is much larger than the vertical scale of the motions which mix the fluid. In the present case, the thickness of the attractor (a few centimetres) should be compared with the water height (20 cm).

The ability of the attractor to mix the fluid can be estimated by computing a turbulent diffusivity during the equilibrium regime. Since this regime is weakly nonlinear, we expect the turbulent diffusivity to be close to the molecular diffusivity, but it is still useful to check this.

In the present case of a uniformly stratified fluid, the turbulent diffusivity is defined by (Winters *et al.* 1995):

$$K_t = \frac{g}{\rho_0} \frac{\phi_d}{N^2}, \quad (5.1)$$

where $\phi_d(z, t)$ is the instantaneous diffusive flux of density due to mixing. Since the fluid is not turbulent in the attractor, ϕ_d may be computed as

$$\phi_d = \kappa \frac{g}{\rho_0} \frac{\overline{|\nabla \tilde{\rho}|^2}}{N^2}, \quad (5.2)$$

where $\tilde{\rho}$ refers to the density field and the overline is a horizontal average. It follows that the turbulent diffusivity can eventually be computed as

$$\frac{K_t}{\kappa} = \left(\frac{g}{\rho_0} \right)^2 \frac{\overline{|\nabla \tilde{\rho}|^2}}{N^4}. \quad (5.3)$$

The ratio K_t/κ in the attractor can easily be estimated from this expression. Decomposing the density field $\tilde{\rho}$ into the initial linear part and the fluctuations yields $K_t/\kappa = 1 + 2\overline{\partial_z b}/N^2 + \overline{|\nabla b|^2}/N^4$. In the attractor, where the changes are dominantly in the cross-direction (i.e. $\partial/\partial s \ll \partial/\partial \eta$), we can write $|\nabla b|^2 \simeq (\partial_\eta b)^2 \simeq (\sin\theta)^{-2}(\partial_z b)^2$. From the colour scale of figure 7, we may take a value of 0.01 as an upper bound for $|\partial_z b|/N^2$ so that $K_t \simeq \kappa$ in the attractor. The same is, of course, true outside the attractor since slow large-scale motions dominate there.

6. Summary and conclusion

The purpose of this paper is to model numerically an internal gravity wave attractor using the MIT general circulation model, to go beyond previous approaches and address questions about nonlinear effects and mixing. For this purpose, the laboratory experiment of HBDM08 is reproduced and a careful comparison with the experimental results is carried out. The geometry of the experiment consists of a trapezoidal tank with a uniform stratification. Despite the two-dimensional configuration of our simulation, very good agreement with the experiment is obtained. The only difference is an insufficient decrease of the amplitude along the attractor and we invoke the absence of lateral boundary layers in the simulation to account for this difference.

We propose a simple model for the thickness of the attractor based upon the opposite effects of viscous diffusion and focusing. This model predicts that the thickness should evolve as the 1/3 power of the ratio of viscous to stratification effects. This agrees well with results by Rieutord *et al.* (2001) and Ogilvie (2005) for rotating fluids (this ratio becoming the Ekman number). When the focusing parameter is larger than about 3 (so that its cube power is much larger than 1),

the expression for the thickness becomes identical to that predicted by Thomas & Stevenson (1972) for a wave beam in the far-field limit. This analogy allows us to interpret the wave attractor as a wave beam emitted by an oscillating source point located at the focusing point.

A linear regime was considered up to this point and the forcing amplitude was increased by a factor 10 to get insight into nonlinear effects and induced mixing. Harmonics at twice the forcing frequency were found, as a result of nonlinear interaction between branches of the attractor, consistent with the prediction of Tabaei *et al.* (2005) for wave beams. The second harmonic motions do not converge toward an attractor and propagate within the closed domain. Third harmonic motions were also found, which are trapped in the attractor because their frequency is larger than the Brunt–Väisälä frequency. Consistently with the weakly nonlinear regime, we found that the turbulent diffusivity within the attractor is hardly larger than the molecular diffusivity.

Several directions of research may be pursued. The simplest one is to consider a nonlinear wave attractor, by increasing again the forcing amplitude. The fate of the attractor in this case is not obvious: harmonics should be produced, which may act as perturbation to the intense vorticity and density layers of the attractor and destabilize them via a Kelvin–Helmholtz instability. Does the attractor form again once the turbulent scales have been dissipated? Also, if the forcing is maintained over a sufficiently long time, induced mixing may modify the background stratification, resulting in a step-like profile which should modify the attractor. The shape of the fluid container has also a strong influence on the attractor, as studied by Maas & Lam (1995) in a linear context. All these simplified approaches are prerequisites before addressing a natural geophysical situation, such as a closed oceanic basin.

We thank Leo Maas who suggested that we model numerically the internal wave attractor. We also thank Jeroen Hazewinkel for having provided an earlier draft of his experimental paper, which greatly helped in the detailed comparison with the simulation. Fruitful discussions with J. Hazewinkel and L. Maas are also acknowledged. Computations were performed on the French Supercomputer Center IDRIS, through contract 070580.

REFERENCES

- BROWAND, F. K., GUYOMAR, D. & YOON, S. C. 1987 The behavior of a oscillating grid. *J. Geophys. Res.* **92**, 5329–5341.
- DRIJFHOUT, S. S. & MAAS, L. R. M. 2007 Impact of channel geometry and rotation on the trapping of internal tides. *J. Phys. Oceanogr.* **37**, 2740–2763.
- GOSTIAUX, L. 2006 Étude expérimentale des ondes de gravité internes: Émission, propagation, réflexion. Thèse de l'École Normale Supérieure de Lyon.
- HAZEWINKEL, J., VAN BREEVOORT, P., DALZIEL, S. B. & MAAS, L. R. M. 2008 Observations on the wave number spectrum and evolution of an internal wave attractor in a two-dimensional basin. *J. Fluid Mech.* **598**, 373–382.
- LAM, F.-P. A. & MAAS, L. R. M. 2008. Internal wave focusing revisited: A reanalysis and new theoretical links. *Fluid Dyn. Res.* **40**, 95–122.
- LIGHTHILL, J. 1978 *Waves in Fluids*. Cambridge University Press.
- MAAS, L. R. M. & LAM, F. P. A. 1995 Geometric focusing of internal waves. *J. Fluid Mech.* **300**, 1–41.
- MAAS, L. R. M., BENIELLI, D., SOMMERIA, J. & LAM, F. P. A. 1997 Observation of an internal wave attractor in a confined, stably stratified fluid. *Nature* **388**, 557–561.

- MARSHALL, J., ADCROFT, A., HILL, C., PERELMAN, L. & HEISEY C. 1997 A finite-volume, incompressible Navier–Stokes model for studies of the ocean on parallel computers. *J. Geophys. Res.* **102**, 5753–5766.
- MCEWAN, A. D. 1971 Degeneration of resonantly-excited standing internal gravity waves. *J. Fluid Mech.* **50**, 431–448.
- MCPHEE-SHAW, E. E. & KUNZE, E. 2002 Boundary-layer intrusions from a sloping bottom: A mechanism for generating intermediate nepheloid layers. *J. Geophys. Res.* **107**, doi:10.1029/2001JC000801.
- OGILVIE, G. I. 2005 Wave attractors and the asymptotic dissipation rate of tidal disturbances. *J. Fluid Mech.* **543**, 19–44.
- PHILLIPS, O. M. 1967 *Dynamics of the Upper Ocean*. Cambridge University Press.
- RIEUTORD, M. & VALDETTARO, L. 1997 Inertial waves in a rotating spherical shell. *J. Fluid Mech.* **341**, 77–99.
- RIEUTORD, M. & NOUI, K. 1999 On the analogy between gravity modes and inertial modes in spherical geometry. *Eur. Phys. J. B* **9**, 731–738.
- RIEUTORD, M., GEORGEOT, B. & VALDETTARO, L. 2001 Inertial waves in a rotating spherical shell: Attractors and asymptotic spectrum. *J. Fluid Mech.* **435**, 104–144.
- RIEUTORD, M., VALDETTARO, L. & GEORGEOT, B. 2002 Analysis of singular inertial modes in a spherical shell: The slender toroidal shell model. *J. Fluid Mech.* **463**, 345–360.
- TABAEI, A., AKYLAS, T. R. & LAMB, K. G. 2005 Nonlinear effects in reflecting and colliding internal wave beams. *J. Fluid Mech.* **526**, 217–243.
- TILGNER, A. 2007 Zonal wind driven by inertial modes. *Phys. Rev. Lett.* **99**, 194501.
- THOMAS, N. H. & STEVENSON, T. N. 1972 A similarity solution for viscous internal waves. *J. Fluid Mech.* **54**, 495–506.
- WINTERS, K. B., LOMBARD, P. N., RILEY, J. J. & D’ASARO, E. A. 1995 Available potential energy and mixing in density-stratified fluids. *J. Fluid Mech.* **289**, 115–128.